Mind the Gap

The Location of the Lower Edge of the Pair-instability Supernova Black Hole Mass Gap

Farmer, R.; Renzo, M.; de Mink, S.E.; Marchant, P.; Justham, S.

[Link to publication](#)

CrossMark

Mind the Gap: The Location of the Lower Edge of the Pair-instability Supernova Black Hole Mass Gap

R. Farmer[1] [iD], M. Renzo[2] [iD], S. E. de Mink[1,3] [iD], P. Marchant[4] [iD], and S. Justham[1,5,6] [iD]

[1] Anton Pannekoek Institute for Astronomy and GRAPPA, University of Amsterdam, NL-1090 GE Amsterdam, The Netherlands; r.j.farmer@uva.nl
[2] Computational Astrophysics, Flatiron Institute, New York, NY 10010, USA
[3] Center for Astrophysics—Harvard & Smithsonian, 60 Garden Street, Cambridge, MA 02138, USA
[4] Center for Interdisciplinary Exploration and Research in Astrophysics (CIERA) and Department of Physics and Astronomy, Northwestern University, 2145 Sheridan Road, Evanston, IL 60208, USA
[5] School of Astronomy & Space Science, University of the Chinese Academy of Sciences, Beijing 100012, People's Republic of China
[6] National Astronomical Observatories, Chinese Academy of Sciences, Beijing 100012, People's Republic of China
Received 2019 August 6; revised 2019 October 25; accepted 2019 October 25; published 2019 December 10

Abstract

Detections of gravitational waves are now starting to probe the mass distribution of stellar mass black holes (BHs). Robust predictions from stellar models are needed to interpret these. Theory predicts the existence of a gap in the BH mass distribution because of pair-instability supernovae. The maximum BH mass below the gap is the result of pulsational mass loss. We evolve massive helium stars through their late hydrodynamical phases of evolution using the open-source MESA stellar evolution code. We find that the location of the lower edge of the mass gap at 45 $M_\odot$ is remarkably robust against variations in the metallicity ($\approx 3\,M_\odot$), the treatment of internal mixing ($\approx 1\,M_\odot$), and stellar wind mass loss ($\approx 4\,M_\odot$), making it the most robust predictor for the final stages of the evolution of massive stars. The reason is that the onset of the instability is dictated by the near-final core mass, which in turn sets the resulting BH mass. However, varying the ^{12}C(α, γ)^{16}O reaction rate within its 1σ uncertainties shifts the location of the gap between 40 $M_\odot$ and 56 $M_\odot$. We provide updated analytic fits for population synthesis simulations. Our results imply that the detection of merging BHs can provide constraints on nuclear astrophysics. Furthermore, the robustness against metallicity suggests that there is a universal maximum for the location of the lower edge of the gap, which is insensitive to the formation environment and redshift for first-generation BHs. This is promising for the possibility to use the location of the gap as a "standard siren" across the universe.

Unified Astronomy Thesaurus concepts: Massive stars (732); Stellar mass loss (1613); Supernovae (1668); Astrophysical black holes (98); Stellar mass black holes (1611); Stellar evolution (1599)

Supporting material: machine-readable table

1. Introduction

The detection of merging black hole (BH) binaries through gravitational waves (e.g., Abbott et al. 2016a, 2019a) has opened an observational window on the most massive stellar BHs in the universe. Stellar evolution theory predicts the existence of a gap in the BH mass distribution due to pair-instability evolution (Fowler & Hoyle 1964; Barkat et al. 1967; Woosley 2017), and the current population of detected binary BHs is consistent with a lack of BHs with masses $\geqslant 45\,M_\odot$ (Abbott et al. 2016a, 2016b, 2017a, 2017b, 2017c). So far, the most massive BH found is the primary of GW170729, with a mass of $50.6^{+16.6}_{-10.2}\,M_\odot$ (Abbott et al. 2019b). This object is at the edge of the theoretically predicted mass gap. Fishbach & Holz (2017) showed that the existence of the gap and the maximum BH mass at its lower edge can be significantly constrained with the detections expected during the third LIGO/Virgo observing run.

The existence of this pair-instability BH mass gap is expected because of the occurrence of pair-instability supernovae (PISNe), which can completely disrupt the progenitor star and leave no compact remnant behind (Rakavy & Shaviv 1967; Fraley 1968; Woosley et al. 2002). However, it is the mass loss during the pulsations in a pulsational pair-instability supernovae (PPISN) that sets the lower edge of this PISN BH mass gap. PPISNe are predicted for stars slightly less massive than PISN progenitors, and they leave behind a BH, but only after having experienced several episodes of pulsational mass loss, which reduce the mass of the final BH. Here, we investigate how robust the location of

the lower edge of the BH mass gap due to PPISNe is (Rakavy & Shaviv 1967; Fraley 1968), i.e., how massive can the most massive BH below the gap be? Single stars with initial masses $100\,M_\odot \lesssim M_{\rm ZAMS} \lesssim 140\,M_\odot$ (or equivalently final helium core masses of $32\,M_\odot \lesssim M_{\rm He} \lesssim 60\,M_\odot$) are expected to undergo pulsation pair instabilities (PPIs) (Woosley et al. 2002; Chen et al. 2014; Yoshida et al. 2016; Woosley 2017; Renzo et al. 2019). This instability results in a series of pulses, each removing mass from the star. Eventually, the core stabilizes, the pulses cease, and the star ends its evolution in an iron core collapse (CC), most likely producing a BH (Barkat et al. 1967; Woosley 2017).

More massive stars are fully disrupted instead of producing ever more massive BHs: for initial masses $140\,M_\odot \lesssim M_{\rm ZAMS} \lesssim 260\,M_\odot$ (metallicity-dependent), corresponding roughly to final helium cores $60\,M_\odot \lesssim M_{\rm He} \lesssim 140\,M_\odot$ (Heger & Woosley 2002), the first pulse is so violent that the entire star is fully disrupted in a PISN (Woosley et al. 2002; Heger et al. 2003), without any BH remnant formed. For even higher initial masses, corresponding to final $M_{\rm He} \gtrsim 130\,M_\odot$, the photodisintegration instability again allows for BH formation (Heger et al. 2003), closing the PISN BH mass gap from above.

From a population of binary BH mergers, we can determine their rate (Abbott et al. 2016b) and their mass distribution (Cutler & Flanagan 1994; Kovetz et al. 2017). However, the timescale for binary BHs to merge can be of the order of gigayears (Paczyński 1967). Therefore, even if it is possible to determine the host galaxy despite the limited spatial localization of binary

BH mergers, the local observed population of stars may have formed later and hence have a different metallicity to that of the BH progenitor. This complicates estimating the rate of BH formation (Portegies Zwart & McMillan 2000; Dominik et al. 2012; Abbott et al. 2016b), since this estimate requires knowing the star formation rate and metallicity evolution of the universe (Madau & Dickinson 2014; Mapelli et al. 2019; Neijssel et al. 2019).

The maximum BH mass below the PISN gap, however, can be more easily determined (Abbott et al. 2019a) because it is independent of the rate of BH formation. We can thus use it without knowing the metallicity-dependent star formation rate of the universe. In this study we explore how sensitive the maximum BH mass is to uncertainties in the metallicity of the progenitors as well as to other known uncertainties in our understanding of stellar physics.

In Section 2 we describe the evolution of PPISNe and PISNe while introducing our computational approach. We outline the parameter variations that we consider in Section 3. In Section 4 we discuss the sensitivity of the maximum BH mass to changes in the metallicity of the stellar progenitors. Section 5 explores how uncertain the maximum BH mass below the PISN mass gap is because of uncertainties in the assumed input physics. We discuss the implications of the maximum BH mass in Section 6. We conclude and summarize our results in Sections 7 and 8.

2. Evolution through the Pulses

Using MESA version[7] 11123 (Paxton et al. 2011, 2013, 2015, 2018, 2019), we evolve a series of single bare helium cores until they undergo either PPI followed by a core-collapse supernova (PPISN) or the more violent pair instability that fully disrupts the star in a PISN. Input files necessary to reproduce this work and the resulting output files are made freely available at www.mesastar.org.[8]

Based on the results of Marchant et al. (2019), we evolve systems around the lower edge of the PISN BH mass gap, with initial helium core masses between 30 and 105 $M_\odot$. We chose to evolve bare helium cores because stars in this mass range are expected to lose their hydrogen-rich envelope long before their death. This could happen either through binary interactions (Kobulnicky & Fryer 2007; Sana et al. 2012; Almeida et al. 2017), strong stellar winds (Vink & de Koter 2005; Renzo et al. 2017), luminous blue variable (LBV)-like mass loss (Humphreys & Davidson 1994), opacity-driven pulsations in the envelope (Moriya & Langer 2015), or because of chemically homogeneous evolution due to fast rotation (Maeder & Meynet 2000; Yoon et al. 2006; de Mink et al. 2009; Mandel & de Mink 2016; Marchant et al. 2016).

As stars evolve from the zero-age helium branch (ZAHB) they proceed by burning helium convectively in their core, which encompasses $\sim$90% of the mass, taking $\sim10^5$ yr. Once helium has been burnt in the core convection ceases, leaving behind a carbon/oxygen (CO) core with an outer helium-burning shell surrounded by a helium-rich surface layer. For sufficiently massive cores an inner region of the star will enter the pair-instability region. Due to dynamical instability from the production of $e^\pm$ pairs softening the equation of state (EOS), the core begins contracting and heating up. Eventually

this region will heat up sufficiently to ignite the residual carbon and explosively ignite the oxygen (Fowler & Hoyle 1964; Barkat et al. 1967; Rakavy & Shaviv 1967).

This ignition will reverse the contraction and may generate an outwardly propagating pulse, if the star was sufficiently massive. As this pulse propagates outward the inner region of the star expands and cools. Once the pulse reaches the surface, it steepens into a shock wave, which can then accelerate material beyond the escape velocity. This removes between a few tenths and a few tens of solar masses of material in a pulsational mass loss episode (PPI) (Yoshida et al. 2016; Marchant et al. 2019; Woosley 2019). Some stars will undergo "weak" pulsations; these stars undergo PPI instabilities but do not drive a shock sufficient to remove mass (Woosley 2017; Marchant et al. 2019). To focus on the impact that this process has on the BH masses, in this study we define only systems that can drive mass loss as undergoing a pulse. We define weak pulses as ones only able to drive small amounts of mass loss, $\approx$0.1 $M_\odot$ per pulse, while strong pulses drive up to several tens of solar masses lost per pulse. The star then contracts and cools either via neutrinos or in the most massive cores undergoing PPIs via radiative energy losses (Woosley 2017; Marchant et al. 2019). This cycle of contraction and ignition can occur multiple times.

This contraction and expansion process is hydrodynamical in nature, generating multiple shocks. To model these shocks we uses MESA's HLLC contact solver (Toro et al. 1994; Paxton et al. 2018) However, for computational reasons we do not use the HLLC solver while the star is in hydrostatic equilibrium. Instead, only as the star evolves away from hydrostatic equilibrium do we switch to using the HLLC solver. We then follow the hydrodynamics through the ignition and expansion of the star. Once all secondary shocks have reached the surface, we excise any material that has a velocity greater than the escape velocity (Yoshida et al. 2016; Marchant et al. 2019). We then create a new stellar model with the same mass, chemical composition, and entropy as the previous model had (minus the excised material). At this point we switch back to using MESA's hydrostatic solver because the star can be approximated as being in hydrostatic equilibrium. This model is then evolved until the next pulse, where this process repeats, or on to CC, which is defined as when any part of the star infalls with $v > 8000$ km s^{-1}. Stars that undergo a PISN are evolved until all stellar material becomes unbound.

We define the time just before a pulse to be when the pressure-weighted integral is $\langle \Gamma_1 \rangle < 4/3$ (Stothers 1999; Marchant et al. 2019). A special case occurs once the core temperature (T_c) exceeds $10^{9.6}$ K, when we continue using the HLLC solver as the star is approaching CC. During the hydrodynamical phases we turn off mass loss from winds. Given the short amount of physical time spent by our models during the hydrodynamical phase of evolution and the typical wind mass loss rates of $\approx10^{-5}$ $M_\odot$ yr^{-1}, this does not significantly influence the final BH masses.

We define the mass of the BH formed to be the mass enclosed with a binding energy $>10^{48}$ erg (e.g., Nadezhin 1980; Lovegrove & Woosley 2013; Fernández et al. 2018) and velocities less than the escape velocity, measured at iron core collapse. Stars that undergo a PISN are expected to be fully disrupted and thus to leave no remnant behind. The final BH mass may depend on the mass of neutrinos lost during the collapse, assuming they are not accreted into the BH (Coughlin et al. 2018). Without a fully consistent theory for BH formation, we use this simple value based on the binding energy, which provides an upper limit on the BH

---

mass. This value of 10^{48} erg is a conservative estimate for the minimum energy released when a star collapses into a BH, due to neutrino emission (Nadezhin 1980; Lovegrove & Woosley 2013; Fernández et al. 2018). In general this limit is $\approx 0.01\ M_\odot$ smaller than the total mass of bound material at CC. We define the location in mass of the CO core at the end of core helium burning as where $X(^{12}C) > 0.01$ and $X(^4He) < 0.01$.

3. Choice of Parameters

There are many uncertain ingredients in the modeling of stars. These can either be algorithmic parameters that are insufficiently constrained by experiments or observations (e.g., convective mixing) or physical quantities that can only be measured in regimes that are much different than the stellar case and require complicated and uncertain extrapolation for their applications to stars (e.g., nuclear reaction rates). Thus we model a range of systems, with differing environmental, physical, and numerical parameters, to test the sensitivity of our results to these parameters.

3.1. Metallicity

Since LIGO has the ability to detect stellar mass BH mergers out to redshifts ≈ 1, for stellar mass BHs, and the potential for the progenitor stars to come from even earlier epochs, it can thus probe the history of star formation across the universe (Abbott et al. 2019a). Thus we evolve a series of models with varying metallicities (Z) between 10^{-5} and 3×10^{-3}. Metallicity primarily effects the evolution of a helium core by varying the amount of mass lost via winds (see Section 3.2), due to the strong dependence on metallicity that mass loss via winds has (Vink et al. 2001; Mokiem et al. 2007). The lower limit results in stars that do not not lose any significant amount of mass through winds. The upper limit is set by the requirement for us to be able to robustly model the PPISN and PISN region. The upper limit used is comparable to the physical upper limit found in Langer et al. (2007) for H-rich PPISN progenitors. At higher metallicities stars lose sufficient mass that they do not enter the pair-instability region and instead evolve in hydrostatic equilibrium through carbon, oxygen, and silicon burning and then undergo direct collapse, likely forming a BH when they try to burn iron. Our fiducial metallicity, when varying other physics parameters, is $Z = 10^{-3}$.

3.2. Wind Mass Loss

The total mass a star loses during its evolution plays a critical role in its fate, but just as important is how and when it loses the mass. Mass loss via winds is not self-consistently solved in 1D models of stellar evolution, but instead is set by a mass loss prescription and that functional form can have a large impact on the star's evolution (Renzo et al. 2017).

We investigate three different algorithms for wind mass loss, each having a different dependence on the stellar properties: the prescription of Hamann et al. (1982, 1995) and Hamann & Koesterke (1998) (H); the prescription of Nugis & Lamers (2000) (N&L); the prescription of Tramper et al. (2016) (T); as well as no mass loss ($\dot{M} = 0$).

The helium cores we investigate have surface luminosities $\approx 10^6\ L_\odot$, which is at the upper edge of currently known Wolf–Rayet stars used to derive these prescriptions. Thus we also append a free scaling factor η to test possible uncertainties in our knowledge of mass loss rates in high-luminosity helium cores.

This free scaling parameter can be related to the inhomogeneities in the wind structure (so-called "clumpiness") with $\eta = \sqrt{\langle \rho^2 \rangle / \langle \rho \rangle^2}$, where ρ is the wind mass density, and the angle brackets indicate the spatial average over the stellar surface. We vary η between 0.1 and 1.0 (Smith 2014), with our fiducial wind being the (H) rate with $\eta = 0.1$ (Yoon et al. 2010). We assume a value of $Z_\odot = 0.014$ (Asplund et al. 2009).

3.3. Neutrino Physics

The evolution of massive stars is governed by neutrino losses: as the star evolves to higher core temperatures and densities the rate of thermal neutrino losses increases. Stars undergoing pulsational instabilities are also sensitive to the neutrino cooling rates, because due to the generation of $e^\pm$ they produce copious amounts of neutrinos from their annihilation, which leads to the core cooling. The stronger the cooling, the more energy is required from nuclear burning to overcome these losses.

MESA implements the analytic fits to neutrino losses from Itoh et al. (1996) for pair, photo, plasma, bremsstrahlung, and recombination neutrino processes. These fits have quoted fitting errors of $\approx 10\%$ for pair, $\approx 1\%$ for photo, $\approx 5\%$ for plasma, and $\approx 10\%$ for recombination neutrinos compared to the detailed calculations for the regions where these processes are dominant (Itoh et al. 1996). Outside the dominant regions the error increases rapidly. Bremsstrahlung neutrino losses have no quoted error, thus we assume $\approx 10\%$ error, similar to the other processes. We test the uncertainty due to this fitting error by varying the neutrino rates by increasing (decreasing) the neutrino loss rate by multiples of the quoted fitting error. While Itoh et al. (1996) states that the analytic fits will generally underpredict the true value, we test both over- and underestimates for completeness.

A second important factor for the rate of neutrino loss in stars is the Weinberg angle, or the weak mixing angle from the Weinberg–Salam theory of the electroweak interaction (Weinberg 1967; Salam 1968). In the analytical fits of Itoh et al. (1996), the Weinberg angle sets the relative rate of neutrino production between neutral current reactions and charged current neutrino reactions. Increasing the Weinberg angle increases the neutrino cooling rate, by increasing the fraction of charged current reactions. While individual measurements of the Weinberg angle have small quoted uncertainties, there is a systematic offset between different values that is larger than the quoted uncertainties. Thus we model three values for the Weinberg angle: 0.2319 (Itoh et al. 1996) (our fiducial value), 0.23867 (Erler & Ramsey-Musolf 2005), and 0.2223 (Mohr et al. 2016). Over the range of Weinberg angles considered here, we find the neutrino rates vary by up to $\approx 3\%$, with the greatest change being in the pair-creation region.

3.4. Mixing

Convection inside a star is a difficult process to model (Böhm-Vitense 1958; Canuto et al. 1996; Meakin & Arnett 2007), especially during dynamical phases of a star's evolution (Chatzopoulos et al. 2014, 2016). Thus, we take a simpler approach and restrict ourselves to testing uncertainties within the framework of mixing length theory (MLT). Specifically, we test the MLT's efficiency parameter α_{MLT} between 1.5 and 2.0, with 2.0 being our fiducial value. While this may not capture the true uncertainty due to convection, it can provide bounds on the result.

We use the prescription of convective velocities from Marchant et al. (2019) to limit the acceleration of convective regions.

At the convective boundaries we assume convective overshoot mixing with an exponential profile. This is parameterized into two terms, f_{ov} and f_0. The first term dictates the scale height of the convective overshoot, in units of the pressure scale height. The second term dictates the starting point inside the convective boundary from where the overshoot begins, in pressure scale heights (Paxton et al. 2011). We assume the value of $f_0 = 0.005$, and vary f_{ov} between 0.0 (no overshooting) and 0.05, with $f_{ov} = 0.01$ being our fiducial value.

3.5. Nuclear Physics

Nuclear reaction rates are highly sensitive to the temperature at which the reaction occurs, and due to this sensitivity the uncertainty in the rate is also highly temperature-dependent (Iliadis et al. 2010a, 2010b; Longland et al. 2010). Varying a nuclear reaction rate within its known uncertainties has been shown to a have large impact on the structure of a star (Hoffman et al. 1999; Iliadis et al. 2002; Fields et al. 2016, 2018).

We vary several nuclear reaction rates between their $\pm 1\sigma$ uncertainties with data from STARLIB (Sallaska et al. 2013). MESA's default set of rates is a combination of NACRE (Angulo et al. 1999) and REACLIB (Cyburt et al. 2010). To sample the rates, we take the median value from STARLIB, and by taking the uncertainty on a rate to be a log-normal distribution we can compute both an upper rate and a lower rate (given by $\pm 1\sigma$) to cover 68% of the rate's probability distribution. These bounds vary as a function of temperature, reflecting the varying uncertainty in the underlying experimental data. When sampling the rates, we vary only one rate at a time, with the remaining ones being taken from NACRE and REACLIB. Correlations between rates can impact the structure of a star and deserve further study (Fields et al. 2016, 2018).

We test variations in three rates; 3α is the triple alpha reaction, C12α is the ^{12}C$(\alpha, \gamma)^{16}$O reaction, and O16α is the ^{16}O$(\alpha, \gamma)^{20}$Ne reaction. We choose to vary only a few rates over their 1σ uncertainties to limit the computational cost.

We also investigate the effect of changing the nuclear network used, which can have a large impact on the evolution of massive stars, due to changes in which isotopes and which reactions are followed (Farmer et al. 2016). By default we use the approx21.net, which follows alpha chain reactions from carbon and iron, and includes compound reactions to follow $(\alpha, p)(p, \gamma)$ reactions (which assumes that the intermediate isotope is in a steady-state equilibrium) (Timmes 1999; Timmes et al. 2000). We also evolve models with both mesa_75.net, which has 75 isotopes up to ^{60}Zn, and mesa_128.net, which has 128 isotopes up to ^{60}Zn, including more neutron-rich nuclei than the mesa_75.net network, which does not include any compound reactions.

3.6. Other Physics

MESA is built upon a range of other physics, which we do not vary here but which can provide other uncertainties in the modeling of massive stars. MESA's EOS for massive stars is a blend of those of OPAL (Rogers & Nayfonov 2002) and HELM (Timmes & Swesty 2000). Radiative opacities are primarily from OPAL (Iglesias & Rogers 1993, 1996), with low-temperature data from Ferguson et al. (2005) and the
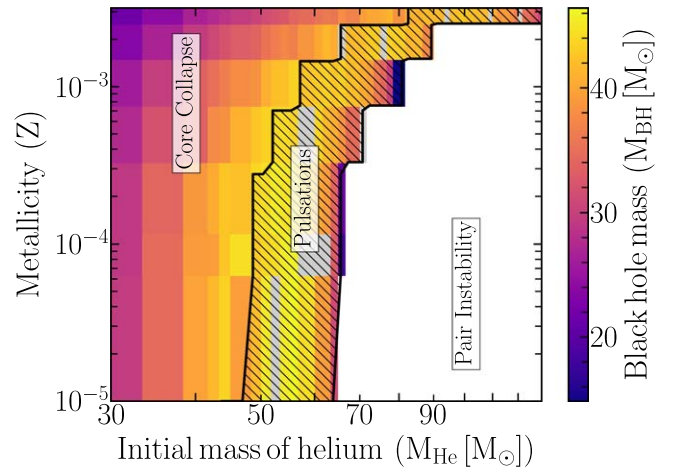

Figure 1. The mass of the BH formed as a function of the metallicity of the star and its initial helium mass. The hashed region denotes those models that undergo pulsational mass loss. Gray regions indicate models that do not reach CC due to numerical issues.

high-temperature, Compton-scattering-dominated regime by Buchler & Yueh (1976). Electron conduction opacities are from Cassisi et al. (2007). Nuclear screening corrections come from Salpeter (1954), Dewitt et al. (1973), Alastuey & Jancovici (1978), and Itoh et al. (1979).

4. Robustness of the Gap to Metallicity

Figure 1 shows the predicted mass of the BH formed from a helium star with a mass between 30 and 100 $M_\odot$ and initial metallicities between $Z = 10^{-5}$ and 3×10^{-3}. At first, as the helium core mass increases, so does the resulting BH mass due to the larger initial mass of the star. However, once the star enters the pulsational regime, it begins to lose mass and eventually the amount of mass loss via pulses is sufficient to lower the final BH mass. This turnover occurs due to changes in the behavior of the PPI pulses. As the core mass increases, the pulses decrease in number but become more energetic, driving off more mass in each pulse. At the edge of the PISN region, the helium cores can lose $\approx 10\,M_\odot$ of material in a single pulse.

As the core mass is increased further, the first pulse becomes energetic enough for the star to be completely disrupted in a PISN. At the lower edge of the BH gap, the most massive helium stars undergoing PPI mass loss without being disrupted lose several tens of solar masses of material per pulse, leaving behind BHs of $\approx 15\,M_\odot$. The lowest mass a BH may have, after undergoing PPISN, is set by the production of ^{56}Ni inside the star. As the initial mass of the star increases, more ^{56}Ni is produced inside it. Eventually sufficient ^{56}Ni is produced to unbind any material that was not initially driven away by the pulses (Marchant et al. 2019). However, the exact edge of the PPISN/PISN boundary, and thus the minimum BH mass produced by a PPISN, is not resolved given our grid spacing.

As the initial metallicity of the star increases, the mass of the BH decreases, for fixed initial helium core mass. This is due to increases in the amount of mass lost via winds before the star enters the PPI region, which decreases the final mass of the star before collapse. The progressive shift to the right of the hatched region in Figure 1 with increasing Z shows that the minimum (and maximum) initial helium core mass needed to undergo pulsations also increases as the metallicity increases. Models
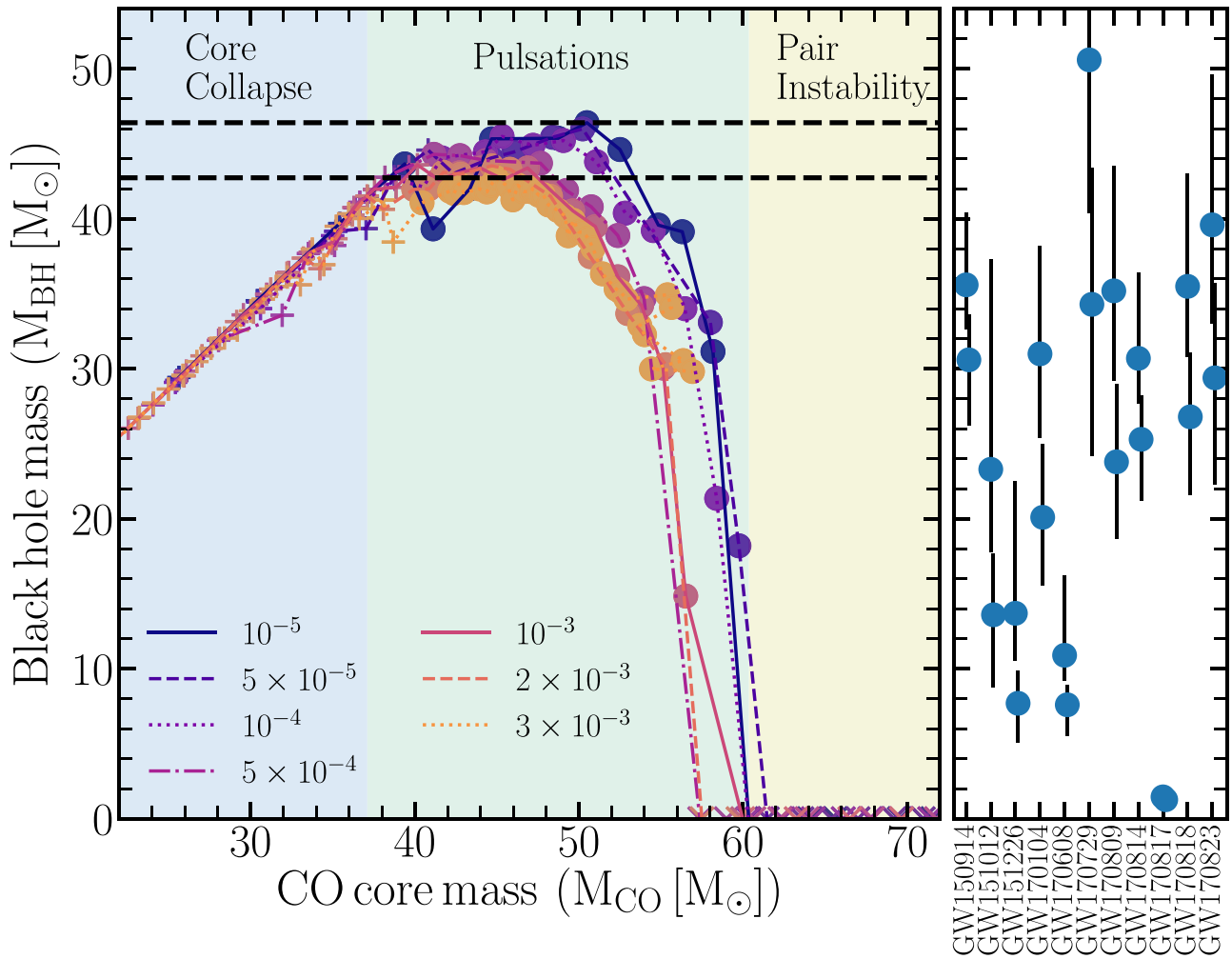
Figure 2. Mass of final BH as a function of the CO core mass for different metallicities. Circles denote models that underwent at least one pulse, pluses evolved directly to CC, and crosses undergo a PISN. The left (blue) region denotes where models undergo CC, the middle (green) region denotes PPISNe, while the right (yellow) region denotes PISNe, as determined by stars with $Z = 10^{-5}$. Points in the right panel show the current median mass estimates for the double compact objects detected by LIGO/VIRGO with their 90% confidence intervals (Abbott et al. 2019a). Dashed horizontal lines emphasize the maximum spread in the locations for the edge of the BH mass gap, or in other words the spread in the maximum BH mass below the PISN BH mass gap.

with $Z \leqslant 3 \times 10^{-3}$ fully populate the regime for pair-instability pulsations. Numerical limitations prevent us from fully populating the PPISN/PISN region at higher metallicities. Thus it may be possible to have PPISNe at higher metallicities, but this would require helium cores initially more massive than $\approx 100\, M_\odot$. Again this is due to the winds; as the winds become stronger we require an initially more massive progenitor star to retain sufficient mass to undergo pulsations.

Figure 2 shows the BH mass as a function of the CO core mass over our metallicity range. Here we see a much tighter relationship between the CO core mass and the final BH mass than in Figure 1 between the initial helium core mass and final BH mass. We find strong PPI pulses removing a significant amount of mass between CO core masses $M_{CO} \approx 38\, M_\odot$ and $M_{CO} \approx 60\, M_\odot$. The upper edge of the PPISN region slightly decreases to $M_{CO} = 56\, M_\odot$ as the metallicity increases. The most massive BHs come from stars with $M_{CO} \approx 50\, M_\odot$, not from those with the most massive CO cores that undergo a PPI (in Figure 1 these are $M_{CO} \approx 60\, M_\odot$). This is due the pulses becoming stronger and thus driving more mass loss.

We attribute the differences arising from changes in metallicity primarily to the differences in wind mass loss rate. Stars with

higher metallicity have higher wind mass loss rates, which increases the amount of mass loss (Castor et al. 1975; Vink et al. 2001). This increased mass loss forces the convective core to recede, leaving behind a smoother composition gradient in the outer layers of the star. At the highest metallicities the stellar winds have also removed all remaining helium from the star and have begun ejecting C/O-rich material in pre-pulses. Thus these progenitors would likely look like carbon- or oxygen-rich Wolf–Rayet (WC/WO) stars before pulsating. This justifies our choice of using the CO core mass over the He core mass as a better proxy for the final BH masses. We note that while the CO–BH mass distribution is fairly constant over the metallicities considered here, the BH formation rate, and hence the merger rate, will vary as a function of metallicity. This is due to changes in the initial stellar mass needed to form such massive CO cores.

The right panel of Figure 2 also shows a comparison with the LIGO/VIRGO BH masses detected by the end of the second observing run (Abbott et al. 2019a, 2019b). We find that the most massive BH LIGO/VIRGO has so far detected is consistent with the upper edge of the BH masses we find. This is due in part to the large 90% confidence intervals on the individual BH masses from GW detections. Nevertheless, even
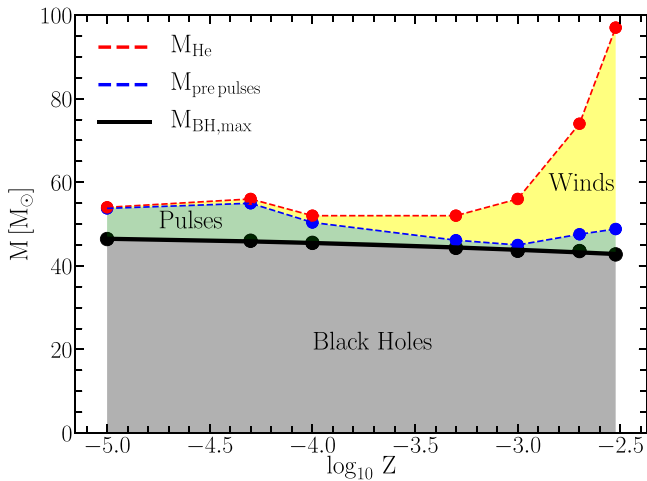
Figure 3. Fate of the mass of the progenitors of the most massive BH below the PISN BH mass gap as a function of metallicity. The gray region denotes mass that becomes the BH. The green region denotes mass that is lost via pulsations. The yellow region denotes mass loss via winds. Black points denote the final BH mass. Blue points denote the edge between mass loss in pulsations and in winds. Red points mark the initial helium core mass of the star.

when considering the much better determined chirp mass of GW170729, it remains below the maximum chirp mass predicted assuming random pairing of BHs with mass ratio $q = M_2/M_1 > 0.5$ (Marchant et al. 2019).

Figure 3 shows, as a function of Z, what is the final fate of the mass inside the progenitor star that forms the most massive BH. At low metallicities, the weakness of the stellar winds results in most of the initial stellar mass of the star forming the BH. At higher metallicities wind mass loss is able to drive approximately half of the initial mass away before the star collapses to form a BH. The stars making the most massive BHs only lose 1–5 $M_\odot$ of material in the pulsations.

Our models span over 2.5 orders of magnitudes in metallicity, but over such a wide range the maximum BH mass decreases only slightly from $M_{BH,Max} = 46\,M_\odot$ to $43\,M_\odot$. This corresponds to a 7% variation over the metallicity range considered here, for BHs whose progenitor underwent a PPISN. The initial helium core mass that forms the most massive BHs at each Z increases from $\approx 54\,M_\odot$ at $Z = 10^{-5}$ to $100\,M_\odot$ at $Z = 3 \times 10^{-3}$. This increase in mass is not due to changes in pulse behavior, but instead to the increased mass loss due to winds (seen as the yellow shaded region in Figure 3). Thus with a change of only 6 $M_\odot$ in BH mass, the initial mass needed to produce the BH changes by $\approx 50\,M_\odot$ because of a change in the metallicity over 2.5 orders of magnitude.

5. Physics Dependence of the Gap

In Figure 4, we show the variations in the BH mass distribution for multiple assumptions of stellar physics, varied within either their theoretical or experimentally derived uncertainties. Each model is computed at a fixed metallicity of $Z = 10^{-3}$, with only one parameter varied in each model.

5.1. Wind Prescription

Figure 4(a) shows the effect of different mass loss prescriptions on the CO–BH mass distribution. Overall the difference in masses between the different prescriptions (and η values) is small. The different prescriptions bifurcate into two groups, those where

$M_{BH,max} \approx 44\,M_\odot$ (H$\eta = 0.1$ and N&L$\eta = 0.1$) and those with $M_{BH,max} \approx 48\,M_\odot$ ($\dot{M} = 0.0$, N&L$\eta = 1.0$, and T (with both values of η)). The models producing smaller maximum BH masses also shift their transition to PISNe to smaller CO core masses. These models lose more mass via winds and come from $M_{He,int} \approx 64\,M_\odot$. The second group, which yield $M_{BH,max} \approx 48\,M_\odot$, come from $M_{He,int} \approx 58\,M_\odot$ cores and lose less mass via winds. As the strength of mass loss increases, either through changing the wind prescription or by increasing the metallicity, the CO–BH mass distribution flattens and decreases the maximum BH mass. There is no set of models (H) with $\eta = 1.0$ shown, because the amount of mass loss when using this prescription is sufficient that no model enters the pulsation region.

5.2. Neutrino Physics

Figure 4(b) shows the BH mass as a function of the CO core mass for variations in the neutrino rate and the Weinberg angle. Over the range of variations in neutrino rates considered here, the effect on the maximum BH mass is small. As the rate increases we find the maximum BH mass varying by $\approx 1\,M_\odot$ and a trend for less massive BHs as the neutrino rate increases. As the Weinberg angle varies, again the CO–BH mass function is approximately constant. Smaller Weinberg angles result in a slightly lower maximum BH mass, with a variation of $\sim 1.5\,M_\odot$ for the range of $\sin^2\theta_W$ considered here.

5.3. Convective Mixing

Figure 4(c) shows variations in α_{MLT} between 1.5 and 2.0, with our default assumption being $\alpha_{MLT} = 2.0$. Within these limits there is very little change in the behavior of the BH masses, with the BH masses slightly decreasing as α_{MLT} increases.

Figure 4(c) also shows the effect of making f_{ov} small. The maximum BH mass varies within 1 $M_\odot$ over the range considered here. The most significant difference occurs at the PPISN/CC boundary, where $f_{ov} = 0.05$ decreases the final BH mass relative to the models with lower f_{ov}. This is due to a change in behavior in the burning and convection regions at the center of the star. When f_{ov} is small the star has a separate off-center burning region and a central one, both of which drive convection zones. When f_{ov} increases, these convection zones can merge, which increases the available fuel supply and causes the pulses to become stronger, driving increased mass loss.

5.4. Nuclear Reaction Rates

Figure 4(d) shows the CO–BH mass function for different rates computed from STARLIB and our default rates from NACRE and REACLIB. Overall the effect of the $^{16}O(\alpha, \gamma)^{20}Ne$ rate is minimal on both the BH mass distribution and the maximum BH mass. However, both the 3α rate and the $^{12}C(\alpha, \gamma)^{16}O$ rate have a large impact on both the BH mass distribution and the maximum BH mass formed.

As the $^{12}C(\alpha, \gamma)^{16}O$ rate decreases the maximum BH mass increases: for $+1\sigma$ we find $M_{BH,max} = 40\,M_\odot$ while at -1σ we find $M_{BH,max} = 58\,M_\odot$. Thus within the 68% confidence interval for the C12α rate the maximum BH mass varies by $\approx 18\,M_\odot$.[9] The median $^{12}C(\alpha, \gamma)^{16}O$ rate from STARLIB, from

---

[9] For $^{12}C(\alpha, \gamma)^{16}O$ reactions with the $+1\sigma$ rate, we burn sufficient ^{12}C during core helium burning that we never trigger the definition of CO core mass in Section 2. Thus we relax our definition of CO core mass to be the mass coordinate at the maximum extent of the convection zone during core helium burning.
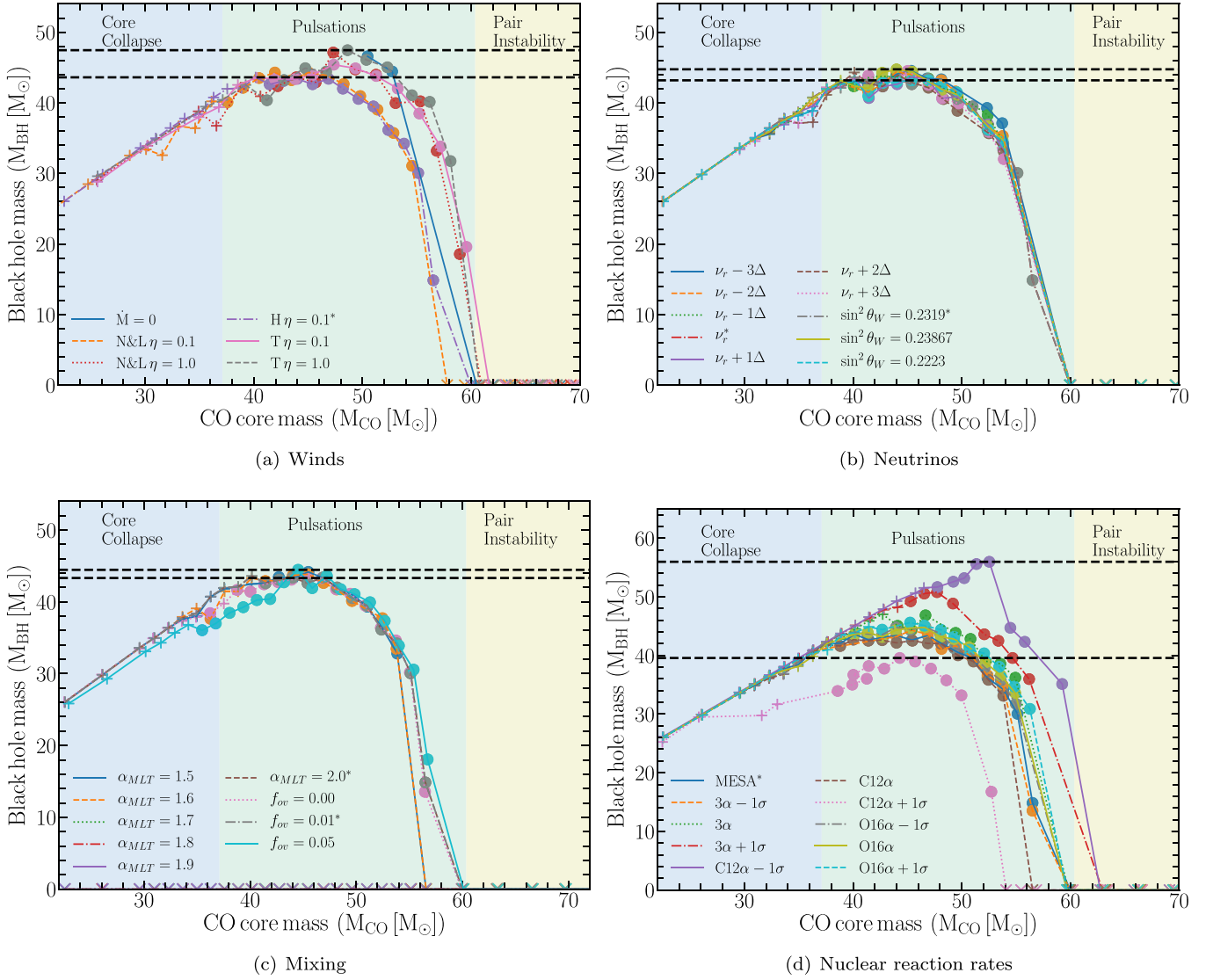
Figure 4. BH mass as function of CO core mass for different physics assumptions. (a) Variations in the wind mass loss prescription; H is the prescription of Hamann & Koesterke ([1998](#)), N&L is that of Nugis & Lamers ([2000](#)), and T is from Tramper et al. ([2016](#)), while η varies between 0.1 and 1.0. (b) Variations in the neutrino physics—due to the numerical uncertainties in the fits (Itoh et al. [1996](#)), each Δ represents a scaling of this fitting error—and the Weinberg angle. (c) Variations in the convective treatment, with varying MLT scale heights α_{MLT} and convective overshoot values f_{ov}. (d) Variations in a select set of nuclear reactions; MESA's default rates are from NACRE (Angulo et al. [1999](#)) and REACLIB (Cyburt et al. [2010](#)), while the other rates come from STARLIB (Sallaska et al. [2013](#)) as either the median or $\pm 1\sigma$ uncertainties; 3α is the triple alpha reaction, C12α is the ^{12}C$(\alpha, \gamma)^{16}$O reaction, and O16α is the ^{16}O$(\alpha, \gamma)^{20}$Ne reaction. Plot symbols have the same meaning as in Figure 2. A star represents our default model assumptions for each physics variation. Dashed lines indicate the range of locations for the edge of the BH mass gap. Colored shading shows the regions between the CC, PPISN, and PISN outcomes for our fiducial set of physics assumptions.

Kunz et al. ([2002](#)), is smaller than the NACRE rate, thus STARLIB predicts a greater maximum BH mass. deBoer et al. ([2017](#)) also provide an updated ^{12}C$(\alpha, \gamma)^{16}$O rate that is smaller, over the temperature range for core helium burning, than NACRE. Models with this rate showed a similar increase in the maximum BH mass.

As the 3α rate, from Angulo et al. ([1999](#)), increases, the maximum BH mass also increases. This correlates with the behavior of the ^{12}C$(\alpha, \gamma)^{16}$O rate; as the 3α rate increases or the ^{12}C$(\alpha, \gamma)^{16}$O rate decreases, we increase the mass fraction of ^{12}C in the core. For the values tested here, this increases from $\approx 10\%$ to $\approx 30\%$.

We find that as the mass fraction of carbon increases in the core the maximum BH mass also increases, and this also alters the behavior of the pulses. Higher carbon fractions

decrease the range in CO core mass within which models undergo pulsations. This would translate into a smaller predicted rate of PPISNe in the universe, because there is a smaller range of possible progenitors. Increasing the mass fraction of carbon also decreases the fraction of models with strong pulsational mass loss, by weakening the pulses such that they do not eject mass. As the carbon fraction increases, the BH mass distribution sharpens (similar to what is seen with no mass loss in Figure [4](#)(a)). This also shifts the boundaries between CC/PPISN and between PPISN/PISN to higher masses as the carbon fraction increases. Moving the boundary between PPISN/PISN to higher CO core masses would translate to needing a more massive initial star, and thus this would decrease the predicted rate of PPISNe and PISNe.

We performed additional tests varying the $^{12}C + ^{12}C$ and $^{16}O + ^{16}O$ reaction rates[10] between 0.1 and 10 times their default MESA values because STARLIB does not have temperature-dependent uncertainties for them. These rates showed variations in the maximum BH mass of $\sim 4\ M_\odot$, with the $^{12}C + ^{12}C$ rate having a larger effect on the maximum BH mass.

Due to the sensitivity of the maximum BH mass to the $^{12}C(\alpha, \gamma)^{16}O$ rate, the measured value of the maximum BH mass (below the PISN mass gap) can be used to place constraints on the $^{12}C(\alpha, \gamma)^{16}O$ rate (R. Farmer et al. 2019, in preparation).

5.5. Model Resolution

MESA has a number of ways to control the spatial and temporal resolution of a model. Here we vary MESA's mesh_delta_coeff, which controls the maximum allowed change in stellar properties between adjacent mesh points during the hydrostatic evolution to between 0.8 and 0.3. Decreasing the value increases the resolution. This range corresponds to an increase by roughly a factor of two in the number of grid points. We also vary MESA's adaptive mesh refinement (AMR) parameters, which set the resolution during hydrodynamical evolution. We vary split_merge_amr_nz_baseline between 6000 and 10,000 and split_merge_amr_nz_MaxLong between 1.25 and 1.15, where the second values denotes a higher resolution. This leads to an increase by a factor of two in the number of spatial zones during the evolution of a pulse.

We have also varied MESA's varcontrol_target, which sets the allowed changes in stellar properties between time steps, between 5×10^{-4} and 5×10^{-5}, and varied max_timestep_factor, which sets the maximum factor by which MESA can increase a time step, between 1.025 and 1.05. This leads to an increase of $\approx 30\%$ in number of time steps taken. Over the ranges considered here we find changes of $\approx 1\ M_\odot$ in the maximum BH mass.

Over the range of nuclear networks considered here—approx21.net, mesa_75.net, mesa_128.net—there is little change in the BH mass for a given CO mass; it changes by at most $\approx 1\ M_\odot$. There is a trend for larger nuclear networks to produce slightly more massive BHs.

Woosley (2017) suggests that PPI systems need large nuclear networks that can adequately follow weak interactions, which approx21.net does not do. However, both the CO–BH mass relationship and the maximum BH mass vary within $\approx 1\ M_\odot$ over the networks considered here. Changing the isotopes evolved will have an effect on the composition and final structure of the star as well as the composition of the ejecta from the pulses. However, we find that much of the behavior that determines the final BH mass is set by the conditions at the initial pulse. These are set by the CO core mass and carbon mass fraction, both of which are set by core helium burning, which is not affected by the lack of weak reactions in approx21.net.

6. The Maximum Black Hole Mass and its Implications

Figure 5 summarizes the range in the maximum BH mass below the PISN gap due to the variations considered in Sections 4 and 5. These include those that are affected by the environment (metallicity) and thus vary across the universe,
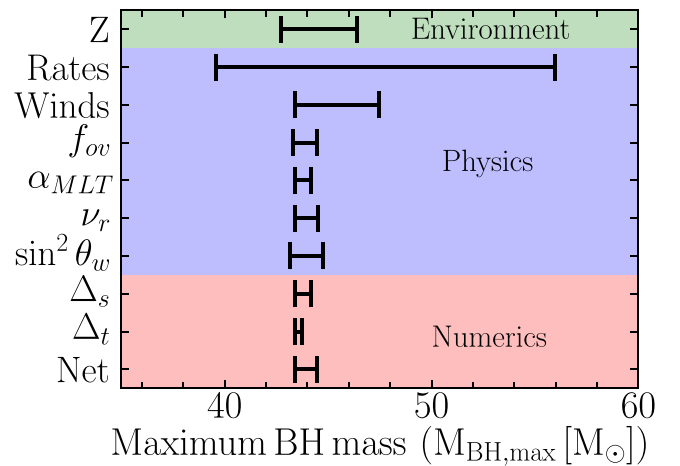

Figure 5. Range of maximum BH masses for different assumptions about the environment and stellar physics. See Figure 2 for the range of metallicities considered here; see Figure 4 for the range of each physics assumption.

those for which we have incomplete or uncertain physics (rates, winds, α_{MLT}, f_{ov}, ν_{rate}, and $\sin^2 \theta_W$) but which we expect to be constant in the universe, and those that are model-dependent (spatial, temporal, and nuclear network resolution). For most of the physics for which we are uncertain (α_{MLT}, f_{ov}, ν_{rate}, and $\sin^2 \theta_W$) and the model resolution (spatial, temporal, and number of isotopes) there is a limited effect on the maximum BH mass. These terms place $\approx 2\ M_\odot$ uncertainties on the maximum BH mass, over the ranges considered here, contingent on how the different uncertainties are combined.

The next most significant factors are the metallicity and winds. We consider these together, since the metallicity dependence of wind mass loss rates introduces a degeneracy between these two elements. We observe a population of BHs from different progenitor stars with varying metallicities, so this 7% variation in the maximum BH mass places a minimum level of uncertainty on what we can learn from the most massive BHs detected. Given a sufficiently large population of binary BHs (at multiple redshifts) it may be possible to disentangle the effects of the star formation and metallicity evolution of the universe on the BH population (Dominik et al. 2013; Dvorkin et al. 2016). However, this uncertainty, which varies across the universe, is small compared to the current measurement uncertainties.

From the detection of a gravitational wave we can infer the luminosity distance to the source. We also obtain the chirp mass in the detector frame, i.e., the redshifted true chirp mass. Knowledge of the true source mass would therefore also provide the redshift to the source, and so allow the use of gravitational wave events to measure the expansion history of the universe without the need for electromagnetic detections to supply the redshift of the event. Knowledge of the edge of the PISN BH mass gap allows BH mergers to act as "standardizable sirens" for cosmology (demonstrated by Farr et al. 2019, following Schutz 1986; Holz & Hughes 2005). The sharper the edge of the PISN mass gap is, the smaller the uncertainty in the derived cosmological parameters that can be achieved (Farr et al. 2019)

The most significant physics variation considered here is due to the nuclear physics uncertainties, and primarily due to the $^{12}C(\alpha, \gamma)^{16}O$ rate, leading to a 40% variation in the maximum BH mass. Models having lower $^{12}C(\alpha, \gamma)^{16}O$ rates lose less

---

[10] In the approx21.net nuclear network these reactions rates are compound rates where the different output channels have been combined.

mass in pulsations and thus produce more massive BHs. Thus, even with a lack of knowledge about the environment in which any individual BH formed, we can still use the detection of sufficiently massive BHs to constrain nuclear physics. The most massive detected BH indicates the maximum value for the $^{12}C(\alpha, \gamma)^{16}O$ rate over the temperature range for core helium burning.

Given the sensitivity of the BH mass to the CO core mass, the maximum BH mass formed is effectively independent of its stellar origin. Assuming that both chemically homogeneous evolution and common envelope evolution can produce a sufficiently massive, H-poor, He core, we would expect those evolutionary scenarios for merging BHs to result in similar final BH masses.

7. Comparisons to Other Work

Yoshida et al. (2016) studied PPISNe from stars with initial masses between 140 and 250 $M_\odot$ and $Z = 0.004$. They find the final masses of their stars to be between 50 and 53 $M_\odot$ at collapse, broadly consistent with the masses we find. For our models at $Z = 0.004$ we would expect slightly smaller BHs, due to the winds stripping the outer CO layers of the stars. Another possible source of differences may be the choice of the $^{12}C(\alpha, \gamma)^{16}O$ rate of Caughlan & Fowler (1988) (Yoshida & Umeda 2011).

Our models agree with the wind-less, metal-free, helium-core models of Woosley (2017), who finds a maximum final BH mass of 48 $M_\odot$. This agrees with our wind-less models where we also find a maximum BH mass of 48 $M_\odot$ (though we evolve them at a non-zero metallicity). Woosley (2017) also finds a maximum BH mass of 52 $M_\odot$ for models that did not remove their entire hydrogen envelope. Although they are not directly comparable to our results, which assume all helium has been removed, they provide bounds on the variation in the maximum BH mass, if the H envelope is not completely removed, of $\approx 4\ M_\odot$. Woosley (2019) investigated the evolution of naked He cores, finding a maximum BH mass below the gap of 46 $M_\odot$, in agreement with our results, for our default $^{12}C(\alpha, \gamma)^{16}O$ rate and assumptions on metallicity.

Takahashi (2018) looked at the effect of varying the $^{12}C(\alpha, \gamma)^{16}O$ rate on the boundary between PPISNe and PISNe. Our results are not directly comparable because they used the rate of Caughlan & Fowler (1988), while by default we use the NACRE rate. They found that as the $^{12}C(\alpha, \gamma)^{16}O$ rate decreases, which increases the ^{12}C fraction, the PISN boundary shifts to higher initial masses, similar to our findings. Takahashi (2018) also finds a narrowing of the PPISN region (in initial mass space), consistent with our results.

Leung et al. (2019) studied the evolution of helium cores in the range 80–140 $M_\odot$ and $Z = 10^{-3}$–$1.0\ Z_\odot$, with a previous MESA release (version 8118) and a different treatment of the hydrodynamics. Their results are in agreement with ours. They find a maximum BH mass of $\approx 50\ M_\odot$, which is larger than what we predict, likely due to their models with the lowest metallicity ($Z = 10^{-2}\ Z_\odot$) having no wind mass loss. Our models with no mass loss at $Z = 10^{-3}$ have a maximum BH mass of 48 $M_\odot$. At higher metallicities we find that wind mass loss is sufficient to make the maximum BH come from a CC event rather than a PPISN. The remaining differences may be due to other differences in the choice of parameters and/or changes between the two MESA versions.

In this work we did not consider the effects of rotation on the stellar progenitors, which is especially important if they came from chemically homogeneous evolution (de Mink et al. 2009; de Mink & Mandel 2016; Marchant et al. 2016). However, Chatzopoulos & Wheeler (2012a, 2012b) have previously studied the impact of rotation on zero-metallicity models evolved first with MESA and then FLASH, in 1D, for the dynamical evolution. They found that increasing the rotation rate causes the initial mass for PPISN or PISN to decrease. This is due to the increase in CO core mass due to rotational mixing. They find PPISNe from stars with core masses of ≈ 40–$65\ M_\odot$, which agrees with our results. However, the impact of centrifugal support on the resulting BH masses from PPISNe is an open problem. Rotation may also affect the final BH mass depending on how the BH is formed and whether material with high angular momentum is accreted into the BH. This may, however, be more relevant for the final spin of the BH rather than the final mass (Fryer & Warren 2004; Rockefeller et al. 2006; Batta et al. 2017).

8. Summary and Conclusions

The prediction of a gap in the mass distribution of BHs from the collapse of stars dates back to the 1960s, when the theory of pair-instability evolution was first developed (Fowler & Hoyle 1964; Barkat et al. 1967). However, it is only recently that the possibility of testing this prediction directly with gravitational waves has opened. As the currently observed population of binary BHs is compatible with having stellar origin (Abbott et al. 2019a, 2019b) instead of dynamical or primordial, we can use models of stellar evolution to interpret the upper end of the BH mass distribution.

We find that the evolution of single bare He cores robustly predicts a maximum BH mass of $\approx 45\ M_\odot$, and that this value is relativity insensitive to variations in the input physics, the algorithmic approach, and the metallicity of the models. In particular, despite the uncertain wind mass loss rates of massive stars, we find a variation of the maximum BH mass of only $\approx 7\%$ (from ≈ 43 to $\approx 46\ M_\odot$) over 2.5 orders of magnitude in metallicity. This implies that detailed knowledge of the host galaxy of merging binary BHs is not required in order to use gravitational wave detections to probe the physics of the unobserved stellar progenitors.

The insensitivity to metallicity of the maximum BH mass below the gap might also allow for cosmological applications. If its value can be determined accurately, it can provide a "standard siren" (Schutz 1986; Holz & Hughes 2005; Farr et al. 2019), allowing estimates of both a redshift and a luminosity distance to the mergers from just the gravitational wave detection.

Assuming a stellar origin, the most massive BHs detected below the pair-instability mass gap might be used to further constrain nuclear physics, specifically the $^{12}C(\alpha, \gamma)^{16}O$ reaction in the core helium-burning regime. In particular, the maximum BH mass puts an upper limit on this reaction rate. Other physics variations including neutrino physics, wind algorithms, and chemical mixing have subdominant effects on the maximum BH mass and negligible contributions to the uncertainty compared to the typical observational uncertainties.

We note, however, that our estimates of the BH mass may be overpredicted if, for instance, a significant amount of mass is loss via neutrinos during the final collapse (Coughlin et al. 2018). Also, our simulations do not account self-consistently

for binary interactions between the progenitor stars, which deserves further attention (Gotberg et al. 2017; Marchant et al. 2019).

If BHs with masses inside the predicted PISN mass gap are detected then either they could have non-stellar origins, they could be the result of multiple mergers in a cluster (Rodriguez et al. 2016; Stone et al. 2017; Di Carlo et al. 2019), or the star could have been H-rich at the time of collapse and then merged in a cluster (Spera et al. 2019; Vigna-Gómez et al. 2019). However, the expected rate of mergers that include a BH in the mass gap is small, due to the requirement that the BHs themselves be the result of previous mergers and that they stayed bound to the cluster after the merger (Gerosa & Berti 2019). Whether BHs are ejected from clusters also depends strongly on whether they are born spinning; if they do not spin then they are more likely to stay bound in the cluster (Rodriguez et al. 2019). If the star can retain its H-rich envelope, by evolving as an isolated single star and then merging with another BH in a dense cluster, then it might be massive enough to enter the mass gap (Woosley 2017). However, the expected rate of mergers in dense clusters is a factor of 40 less than the expected rate of isolated binary mergers (Belczynski et al. 2016b; Rodriguez et al. 2016).

The present and upcoming detections of binary BH mergers might provide evidence constraining the death of the most massive stars before we might be able to unequivocally observe these phenomena in the electromagnetic spectrum (Stevenson et al. 2019). Our results suggest that, with a large population of merger events, we can put constraints on uncertain nuclear physics and provide a new tool for cosmology.

Appendix A
Analytic Fits for Population Synthesis

Population synthesis studies of the impact of PPI on the distribution of mergers detected via gravitational waves have relied on numerical fits to the results of Woosley (2017) expressed as a function of the helium core mass (e.g., Belczynski et al. 2016a; Spera & Mapelli 2017; Stevenson et al. 2019). However, at high metallicities we find that the stars are stripped of all helium, leaving a bare CO core. As the CO core mass at the time of CC is a quantity that is available in population synthesis calculations (although possibly defined in a different way to here, Hurley et al. 2000), we recommend to use M_{CO} as the independent variable to determine the final BH mass of stars, although this only applies to stars that have lost their hydrogen envelopes either in binary interactions or due to wind mass loss.

For any given choice of physics and numerics, the second most important parameter, after M_{CO}, in determining the final BH mass is the initial metallicity of the star, Z. We provide an approximate fit to the BH masses in Figure 2 in terms of these two parameters:

$$M_{BH} = \begin{cases} 4 + M_{CO} & M_{CO} < 38 \\ a_1 M_{CO}^2 + a_2 M_{CO} + a_3 \log_{10}(Z) + a_4 & 38 \leqslant M_{CO} \leqslant 60 \\ 0.0 & 60 < M_{CO} \end{cases}$$
(1)

where $a_1 = -0.096$, $a_2 = 8.564$, $a_3 = -2.07$, and $a_4 = -152.97$, and all masses are in units of $M_\odot$ and accurate to $\approx 20\%$, though the accuracy of the fit decreases as the metallicity decreases.

We note that for $M_{CO} < 38 \, M_\odot$ weak pulses that do not result in significant mass ejection are still possible and might have an effect on the orbital properties of a binary system (e.g., Marchant et al. 2019). Moreover, the fit of Equation (1) does not contain information on the mass lost by each individual pulse or on the timing of the pulses, both of which might influence the evolution in a binary.

Another important result of this study is the small sensitivity of the maximum BH mass below the pair-instability gap to metallicity, with only a $\approx 7\%$ variation over a range in Z spanning 2.5 orders of magnitude. Therefore, the maximum BH mass might be used as a "standard siren" for cosmological applications once sufficiently large samples of BHs are detected. We also provide an approximate fit to the maximum BH mass below the pair-instability gap as a function of the metallicity, which expresses this weak dependence:

$$M_{BH,max} = b_1 + b_2 \log_{10}(Z) + b_3 [\log_{10}(Z)]^2$$
(2)

where $b_1 = 35.1$, $b_2 = -3.9$, and $b_3 = -0.32$, and the resulting $M_{BH, max}$ is in solar units and accurate to $\approx 3\%$. This can be applied also to metallicities $Z < 10^{-5}$, lower than considered here, since we do not expect significant (line-driven) wind mass loss in this regime. However, it is unlikely to be valid for stars with $Z > 3 \times 10^{-3}$, due to their stronger winds that prevent the formation of sufficiently massive CO cores to experience PPI-driven mass loss.

Table 1
Fate of the Mass of the Progenitors for Our Fiducial Model

Parameter	Value	M_{int}	M_{He}	M_{CO}	M_{BH}	ΔM_{pulse}	ΔM_{wind}	ΔM_{SN}	Fate
Z	10^{-3}	30	26.12	22.55	26.05	0.00	3.88	0.08	CC
		35	29.94	26.09	29.85	0.00	5.06	0.10	CC
		40	33.66	29.57	33.60	0.00	6.34	0.06	CC
		42	35.12	30.98	34.97	0.00	6.88	0.15	CC
		44	36.57	32.32	36.43	0.00	7.43	0.14	CC
		46	38.00	33.64	37.78	0.00	8.00	0.22	CC
		48	39.42	34.95	38.38	0.00	8.58	1.04	CC
		50	40.83	36.30	40.76	0.00	9.17	0.08	CC
		52	42.23	37.55	41.97	0.00	9.77	0.26	CC
		54	43.62	38.86	42.10	0.00	10.38	1.52	CC
		56	44.99	40.16	43.60	0.00	11.01	1.39	CC
		58	46.36	41.45	42.61	3.55	11.64	0.20	PPISN
		60	47.71	42.73	43.08	4.33	12.29	0.30	PPISN
		62	49.06	44.00	43.39	4.66	12.94	1.01	PPISN
		64	50.39	45.40	42.62	6.63	13.61	1.14	PPISN
		66	51.73	46.88	43.40	7.83	14.27	0.50	PPISN
		68	53.04	48.19	42.00	10.27	14.96	0.78	PPISN
		70	54.36	49.63	40.54	12.87	15.64	0.94	PPISN
		72	55.70	51.00	39.49	15.24	16.30	0.97	PPISN
		74	56.96	52.37	36.14	19.22	17.04	1.59	PPISN
		76	58.25	53.82	34.21	23.26	17.75	0.78	PPISN
		78	59.55	55.13	30.05	26.74	18.45	2.76	PPISN
		80	60.83	56.51	14.85	45.88	19.17	0.11	PPISN
		85	64.02	59.98	0.00	64.02	20.98	0.00	PISN
		90	67.09	63.24	0.00	67.09	22.91	0.00	PISN
		95	70.12	66.51	0.00	70.12	24.88	0.00	PISN
		100	73.10	69.66	0.00	73.10	26.90	0.00	PISN
		105	76.05	72.80	0.00	76.05	28.95	0.00	PISN
		110	78.95	75.88	0.00	78.95	31.05	0.00	PISN

(This table is available in its entirety in machine-readable form.)

Appendix B
Mass Loss from Progenitors

Table 1 shows the amount of mass loss and the final fate for our fiducial set of stellar parameters. A full version of the table for all models is available online for the other parameters considered here. Table 1 shows: the initial (helium) mass; the helium and carbon/oxygen core masses, measured before the pulsations begin; the final BH mass; the mass lost in pulses; the mass loss in winds; the mass lost in the final supernova; and the final fate of the star. The mass lost in the supernova is a combination of the mass loss due to material having a binding energy $<10^{48}$ erg (Nadezhin 1980; Lovegrove & Woosley 2013; Fernández et al. 2018) and material that is in the process of being ejected (i.e., it is moving faster than the local escape velocity) but has not been removed from the model at the time of core collapse.

ORCID iDs

R. Farmer ⓘ https://orcid.org/0000-0003-3441-7624
M. Renzo ⓘ https://orcid.org/0000-0002-6718-9472
S. E. de Mink ⓘ https://orcid.org/0000-0001-9336-2825
P. Marchant ⓘ https://orcid.org/0000-0002-0338-8181
S. Justham ⓘ https://orcid.org/0000-0001-7969-1569

References

Abbott, B. P., Abbott, R., Abbott, T. D., et al. 2016a, PhRvL, 116, 061102
Abbott, B. P., Abbott, R., Abbott, T. D., et al. 2016b, ApJL, 818, L22
Abbott, B. P., Abbott, R., Abbott, T. D., et al. 2017a, PhRvL, 118, 221101
Abbott, B. P., Abbott, R., Abbott, T. D., et al. 2017b, ApJL, 851, L35
Abbott, B. P., Abbott, R., Abbott, T. D., et al. 2017c, PhRvL, 119, 141101
Abbott, B. P., Abbott, R., Abbott, T. D., et al. 2019a, PhRvX, 9, 031040
Abbott, B. P., Abbott, R., Abbott, T. D., et al. 2019b, ApJL, 882, L24
Alastuey, A., & Jancovici, B. 1978, ApJ, 226, 1034
Almeida, L. A., Sana, H., Taylor, W., et al. 2017, A&A, 598, A84
Angulo, C., Arnould, M., Rayet, M., et al. 1999, NuPhA, 656, 3
Asplund, M., Grevesse, N., Sauval, A. J., & Scott, P. 2009, ARA&A, 47, 481
Barkat, Z., Rakavy, G., & Sack, N. 1967, PhRvL, 18, 379
Batta, A., Ramirez-Ruiz, E., & Fryer, C. 2017, ApJL, 846, L15
Belczynski, K., Heger, A., Gladysz, W., et al. 2016a, A&A, 594, A97
Belczynski, K., Holz, D. E., Bulik, T., & O'Shaughnessy, R. 2016b, Natur, 534, 512
Böhm-Vitense, E. 1958, ZA, 46, 108
Buchler, J. R., & Yueh, W. R. 1976, ApJ, 210, 440
Canuto, V. M., Goldman, I., & Mazzitelli, I. 1996, ApJ, 473, 550
Cassisi, S., Potekhin, A. Y., Pietrinferni, A., Catelan, M., & Salaris, M. 2007, ApJ, 661, 1094
Castor, J. I., Abbott, D. C., & Klein, R. I. 1975, ApJ, 195, 157
Caughlan, G. R., & Fowler, W. A. 1988, ADNDT, 40, 283
Chatzopoulos, E., Couch, S. M., Arnett, W. D., & Timmes, F. X. 2016, ApJ, 822, 61
Chatzopoulos, E., Graziani, C., & Couch, S. M. 2014, ApJ, 795, 92
Chatzopoulos, E., & Wheeler, J. C. 2012a, ApJ, 748, 42
Chatzopoulos, E., & Wheeler, J. C. 2012b, ApJ, 760, 154
Chen, K.-J., Woosley, S., Heger, A., Almgren, A., & Whalen, D. J. 2014, ApJ, 792, 28
Coughlin, E. R., Quataert, E., Fernández, R., & Kasen, D. 2018, MNRAS, 477, 1225
Cutler, C., & Flanagan, É. E. 1994, PhRvD, 49, 2658
Cyburt, R. H., Amthor, A. M., Ferguson, R., et al. 2010, ApJS, 189, 240
de Mink, S. E., Cantiello, M., Langer, N., et al. 2009, A&A, 497, 243
de Mink, S. E., & Mandel, I. 2016, MNRAS, 460, 3545
deBoer, R. J., Görres, J., Wiescher, M., et al. 2017, RvMP, 89, 035007
Dewitt, H. E., Graboske, H. C., & Cooper, M. S. 1973, ApJ, 181, 439
Di Carlo, U. N., Giacobbo, N., Mapelli, M., et al. 2019, MNRAS, 487, 2947

Dominik, M., Belczynski, K., Fryer, C., et al. 2012, ApJ, 759, 52
Dominik, M., Belczynski, K., Fryer, C., et al. 2013, ApJ, 779, 72
Dvorkin, I., Vangioni, E., Silk, J., Uzan, J.-P., & Olive, K. A. 2016, MNRAS, 461, 3877
Erler, J., & Ramsey-Musolf, M. J. 2005, PhRvD, 72, 073003
Farmer, R. 2019, rjfarmer/mesaplot: Bug fixes, v1.0.7, Zenodo, doi:10.5281/zenodo.3515246
Farmer, R., Fields, C. E., Petermann, I., et al. 2016, ApJS, 227, 22
Farr, W. M., Fishbach, M., Ye, J., & Holz, D. 2019, ApJL, 883, L42
Ferguson, J. W., Alexander, D. R., Allard, F., et al. 2005, ApJ, 623, 585
Fernández, R., Quataert, E., Kashiyama, K., & Coughlin, E. R. 2018, MNRAS, 476, 2366
Fields, C. E., Farmer, R., Petermann, I., Iliadis, C., & Timmes, F. X. 2016, ApJ, 823, 46
Fields, C. E., Timmes, F. X., Farmer, R., et al. 2018, ApJS, 234, 19
Fishbach, M., & Holz, D. E. 2017, ApJL, 851, L25
Fowler, W. A., & Hoyle, F. 1964, ApJS, 9, 201
Fraley, G. S. 1968, Ap&SS, 2, 96
Fryer, C. L., & Warren, M. S. 2004, ApJ, 601, 391
Gerosa, D., & Berti, E. 2019, PhRvD, 100, 041301
Gotberg, Y., de Mink, S. E., & Groh, J. H. 2017, A&A, 608, A11
Hamann, W. R., & Koesterke, L. 1998, A&A, 335, 1003
Hamann, W.-R., Koesterke, L., & Wessolowski, U. 1995, A&A, 299, 151
Hamann, W.-R., Schoenberner, D., & Heber, U. 1982, A&A, 116, 273
Heger, A., Fryer, C. L., Woosley, S. E., Langer, N., & Hartmann, D. H. 2003, ApJ, 591, 288
Heger, A., & Woosley, S. E. 2002, ApJ, 567, 532
Hoffman, R. D., Woosley, S. E., Weaver, T. A., Rauscher, T., & Thielemann, F. K. 1999, ApJ, 521, 735
Holz, D. E., & Hughes, S. A. 2005, ApJ, 629, 15
Humphreys, R. M., & Davidson, K. 1994, PASP, 106, 1025
Hunter, J. D. 2007, CSE, 9, 90
Hurley, J. R., Pols, O. R., & Tout, C. A. 2000, MNRAS, 315, 543
Iglesias, C. A., & Rogers, F. J. 1993, ApJ, 412, 752
Iglesias, C. A., & Rogers, F. J. 1996, ApJ, 464, 943
Iliadis, C., Champagne, A., José, J., Starrfield, S., & Tupper, P. 2002, ApJS, 142, 105
Iliadis, C., Longland, R., Champagne, A. E., & Coc, A. 2010a, NuPhA, 841, 251
Iliadis, C., Longland, R., Champagne, A. E., Coc, A., & Fitzgerald, R. 2010b, NuPhA, 841, 31
Itoh, N., Hayashi, H., Nishikawa, A., & Kohyama, Y. 1996, ApJS, 102, 411
Itoh, N., Totsuji, H., Ichimaru, S., & Dewitt, H. E. 1979, ApJ, 234, 1079
Kluyver, T., Ragan-Kelley, B., Pérez, F., et al. 2016, in Positioning and Power in Academic Publishing: Players, Agents and Agendas: Proc. 20th Int. Conf. on Electronic Publishing, ed. F. Loizides & B. Schmidt (Amsterdam: IOS Press), 87
Kobulnicky, H. A., & Fryer, C. L. 2007, ApJ, 670, 747
Kovetz, E. D., Cholis, I., Breysse, P. C., & Kamionkowski, M. 2017, PhRvD, 95, 103010
Kunz, R., Fey, M., Jaeger, M., et al. 2002, ApJ, 567, 643
Langer, N., Norman, C. A., de Koter, A., et al. 2007, A&A, 475, L19
Leung, S.-C., Nomoto, K., & Blinnikov, S. 2019, arXiv:1901.11136
Longland, R., Iliadis, C., Champagne, A. E., et al. 2010, NuPhA, 841, 1
Lovegrove, E., & Woosley, S. E. 2013, ApJ, 769, 109
Madau, P., & Dickinson, M. 2014, ARA&A, 52, 415
Maeder, A., & Meynet, G. 2000, ARA&A, 38, 143
Mandel, I., & de Mink, S. E. 2016, MNRAS, 458, 2634
Mapelli, M., Giacobbo, N., Santoliquido, F., & Artale, M. C. 2019, MNRAS, 487, 2

Marchant, P., Langer, N., Podsiadlowski, P., Tauris, T. M., & Moriya, T. J. 2016, A&A, 588, A50
Marchant, P., Renzo, M., Farmer, R., et al. 2019, ApJ, 882, 36
Meakin, C. A., & Arnett, D. 2007, ApJ, 667, 448
Mohr, P. J., Newell, D. B., & Taylor, B. N. 2016, RvMP, 88, 035009
Mokiem, M. R., de Koter, A., Vink, J. S., et al. 2007, A&A, 473, 603
Moriya, T. J., & Langer, N. 2015, A&A, 573, A18
Nadezhin, D. K. 1980, Ap&SS, 69, 115
Neijssel, C. J., Vigna-Gómez, A., Stevenson, S., et al. 2019, MNRAS, 490, 3740
Nugis, T., & Lamers, H. J. G. L. M. 2000, A&A, 360, 227
Paczyński, B. 1967, AcA, 17, 287
Paxton, B., Bildsten, L., Dotter, A., et al. 2011, ApJS, 192, 3
Paxton, B., Cantiello, M., Arras, P., et al. 2013, ApJS, 208, 4
Paxton, B., Marchant, P., Schwab, J., et al. 2015, ApJS, 220, 15
Paxton, B., Schwab, J., Bauer, E. B., et al. 2018, ApJS, 234, 34
Paxton, B., Smolec, R., Schwab, J., et al. 2019, ApJS, 243, 10
Pérez, F., & Granger, B. E. 2007, CSE, 9, 21
Portegies Zwart, S. F., & McMillan, S. L. W. 2000, ApJL, 528, L17
Rakavy, G., & Shaviv, G. 1967, ApJ, 148, 803
Renzo, M., Farmer, R., Justham, S., et al. 2019, MNRAS, submitted
Renzo, M., Ott, C. D., Shore, S. N., & de Mink, S. E. 2017, A&A, 603, A118
Rockefeller, G., Fryer, C. L., & Li, H. 2006, arXiv:astro-ph/0608028
Rodriguez, C. L., Chatterjee, S., & Rasio, F. A. 2016, PhRvD, 93, 084029
Rodriguez, C. L., Zevin, M., Amaro-Seoane, P., et al. 2019, PhRvD, 100, 043027
Rogers, F. J., & Nayfonov, A. 2002, ApJ, 576, 1064
Salam, A. 1968, in Elementary Particle Theory. Relativistic Groups and Analyticity, ed. N. Svartholm (Stockholm: Almqvist & Wiksell), 367
Sallaska, A. L., Iliadis, C., Champange, A. E., et al. 2013, ApJS, 207, 18
Salpeter, E. E. 1954, AuJPh, 7, 373
Sana, H., de Mink, S. E., de Koter, A., et al. 2012, Sci, 337, 444
Schutz, B. F. 1986, Natur, 323, 310
Smith, N. 2014, ARA&A, 52, 487
Spera, M., & Mapelli, M. 2017, MNRAS, 470, 4739
Spera, M., Mapelli, M., Giacobbo, N., et al. 2019, MNRAS, 485, 889
Stevenson, S., Sampson, M., Powell, J., et al. 2019, ApJ, 882, 121
Stone, N. C., Metzger, B. D., & Haiman, Z. 2017, MNRAS, 464, 946
Stothers, R. B. 1999, MNRAS, 305, 365
Takahashi, K. 2018, ApJ, 863, 153
Timmes, F. X. 1999, ApJS, 124, 241
Timmes, F. X., Hoffman, R. D., & Woosley, S. E. 2000, ApJS, 129, 377
Timmes, F. X., & Swesty, F. D. 2000, ApJS, 126, 501
Toro, E. F., Spruce, M., & Speares, W. 1994, ShWav, 4, 25
Townsend, R. 2018, MESA SDK for Linux, Zenodo, doi:10.5281/zenodo.2603170
Tramper, F., Sana, H., & de Koter, A. 2016, ApJ, 833, 133
van der Walt, S., Colbert, S. C., & Varoquaux, G. 2011, CSE, 13, 22
Vigna-Gómez, A., Justham, S., Mandel, I., de Mink, S. E., & Podsiadlowski, P. 2019, ApJL, 876, L29
Vink, J. S., & de Koter, A. 2005, A&A, 442, 587
Vink, J. S., de Koter, A., & Lamers, H. J. G. L. M. 2001, A&A, 369, 574
Weinberg, S. 1967, PhRvL, 19, 1264
Woosley, S. E. 2017, ApJ, 836, 244
Woosley, S. E. 2019, ApJ, 878, 49
Woosley, S. E., Heger, A., & Weaver, T. A. 2002, RvMP, 74, 1015
Yoon, S.-C., Langer, N., & Norman, C. 2006, A&A, 460, 199
Yoon, S.-C., Woosley, S. E., & Langer, N. 2010, ApJ, 725, 940
Yoshida, T., & Umeda, H. 2011, MNRAS, 412, L78
Yoshida, T., Umeda, H., Maeda, K., & Ishii, T. 2016, MNRAS, 457, 351